

**Atmospheric  
correction of  
thermal-infrared  
imagery**

F. Meier et al.

This discussion paper is/has been under review for the journal Atmospheric Measurement Techniques (AMT). Please refer to the corresponding final paper in AMT if available.

# Atmospheric correction of thermal-infrared imagery of the 3-D urban environment acquired in oblique viewing geometry

F. Meier<sup>1</sup>, D. Scherer<sup>1</sup>, J. Richters<sup>2</sup>, and A. Christen<sup>3</sup>

<sup>1</sup>Technische Universität Berlin, Department of Ecology, Chair of Climatology, Rothenburgstraße 12, 12165 Berlin, Germany

<sup>2</sup>Lohmeyer Consulting Engineers GmbH & Co. KG, Karlsruhe, Germany

<sup>3</sup>University of British Columbia, Department of Geography & Atmospheric Science Program, Vancouver, Canada

Received: 7 October 2010 – Accepted: 29 November 2010 – Published: 13 December 2010

Correspondence to: F. Meier (fred.meier@tu-berlin.de)

Published by Copernicus Publications on behalf of the European Geosciences Union.

Title Page

Abstract

Introduction

Conclusions

References

Tables

Figures

⏪

⏩

◀

▶

Back

Close

Full Screen / Esc

Printer-friendly Version

Interactive Discussion

## Abstract

This research quantifies and discusses atmospheric effects that alter the radiance observed by a ground-based thermal-infrared (TIR) camera mounted on top of a high-rise building in the city of Berlin, Germany. The study shows that atmospheric correction of ground-based TIR imagery of the three-dimensional (3-D) urban environment acquired in oblique viewing geometry has to account for spatial variability of line-of-sight (LOS) geometry. We present an atmospheric correction procedure that uses these spatially distributed LOS geometry parameters, the radiative transfer model MODTRAN 5.2 and atmospheric profile data derived from meteorological measurements in the field of view (FOV) of the TIR camera. The magnitude of atmospheric effects varies during the analysed 24-hourly period (8 August 2009) and is particularly notable for surfaces showing a strong surface-to-air temperature difference. The differences between uncorrected and corrected TIR imagery reach up to 7.7 K at 12:00. Atmospheric effects are biased up to 4.3 K at 12:00 and up to 0.6 K at 24:00, if non-spatially distributed LOS parameters are used.

## 1 Introduction

Surface temperature is a key variable in the study of energy and mass exchange at the surface-atmosphere interface. The combination of natural and anthropogenic three-dimensional (3-D) objects in urban areas results in strong spatial and temporal heterogeneity of surface temperatures of urban facets (Voogt and Oke, 1998; Lagouarde and Irvine, 2008; Lagouarde et al., 2010). Thermal-infrared (TIR) remote sensing approaches, which allow the derivation of surface temperatures, have been widely applied in urban climate studies (Voogt and Oke, 2003; Weng, 2009) and were part of several integrated field campaigns like BUBBLE (Rotach et al., 2005), ESCOMPOTE (Mestayer et al., 2005) and CAPITOU (Masson et al., 2008).

### Atmospheric correction of thermal-infrared imagery

F. Meier et al.

Title Page

Abstract

Introduction

Conclusions

References

Tables

Figures



Back

Close

Full Screen / Esc

Printer-friendly Version

Interactive Discussion



**Atmospheric  
correction of  
thermal-infrared  
imagery**

F. Meier et al.

Title Page

Abstract

Introduction

Conclusions

References

Tables

Figures

◀

▶

◀

▶

Back

Close

Full Screen / Esc

Printer-friendly Version

Interactive Discussion



With respect to urban climate research, low cost and high-resolution TIR camera systems mounted on towers or building roofs provide an alternative to airborne and satellite platforms (Voogt and Oke, 2003). Ground-based TIR remote sensing approaches were part of several studies addressing the energy exchange in urban areas. For instance, Hoyano et al. (1999) used time-sequential thermography (TST) for calculating sensible heat flux density at the building scale. In Tokyo, a TIR camera measured urban surface temperatures from the top of a high-rise building for derivation of a local-scale thermal property parameter (Sugawara et al., 2001). Further ground-based studies used TST for the assessment of thermal characteristics of various urban surfaces (Chudnovsky et al., 2004), to study spatio-temporal differences between surface and air temperature as an important boundary condition for ventilation of the urban canopy layer by buoyancy effects (Yang and Li, 2009), or to study spatio-temporal persistence of shadow effects and surface thermal admittance (Meier et al., 2010).

However, radiative processes in the atmosphere between surface and sensor have an impact on remote sensing data. In the TIR part of the electromagnetic spectrum, atmospheric effects that alter the radiance observed by the sensor include absorption and emission primarily induced by water vapour, carbon dioxide and ozone. These atmospheric effects can lead to temperature differences between true surface temperature and remotely sensed values recorded by the sensor larger than 10 K (Jacob et al., 2003).

Several methods are available to remove these atmospheric effects depending on sensor characteristics e.g. the split window technique for multi-channel sensors (Price, 1984; Becker and Li, 1990; Sobrino et al., 1991; Kerr et al., 1992) or the use of radiative transfer models coupled with atmospheric profile data on pressure, temperature and humidity adequate for multi and single-channel sensors (Berk et al., 1998; Schmugge et al., 1998; Richter and Schläpfer, 2002). While these methods are common for data derived from satellite (Prata et al., 1995; Dash et al., 2002) or airborne platforms (Jacob et al., 2003; Lagouarde et al., 2004; Lagouarde and Irvine, 2008), the need for atmospheric correction of ground-based TIR imagery acquired in oblique view is an

open question insofar as the 3-D urban form is concerned.

Only a few ground-based studies account for atmospheric effects. They include either the use of a radiative transfer model to determine a linear relation between observed and corrected surface temperature for target-sensor distances of selected region of interests (Sugawara et al., 2001) or the assumption of a global sensor-target distance and atmospheric transmission value (Yang and Li, 2009).

The objective of this paper is to present a comprehensive atmospheric correction procedure for ground-based single-channel TIR sensors that works on a pixel-by-pixel basis considering the 3-D form of the urban environment and resulting differences in line-of-sight (LOS) geometry due to an oblique viewing geometry. We give answers on how to derive view zenith angle ( $\theta_j$ ), surface height a.s.l. ( $z_j^{\text{surf}}$ ) and sensor-target distances for every image pixel  $j$ . Further we quantify the magnitude of atmospheric effects on the TST data in the study area during a diurnal cycle using the atmospheric radiative transfer model MODTRAN 5.2 (MOD5) (Berk et al., 2005) coupled with profile data from temperature and humidity measurements in the field of view (FOV) of the TIR camera.

Section 2 describes the theoretical background and shows possible atmospheric effects on off-nadir TIR remote sensing in urban areas with the help of a fictitious experimental setup and MOD5 simulations. In the third section, we describe the study site, our experimental setup, pre-processing steps of TIR imagery, LOS parameter determination and the atmospheric correction procedure. Section 4 presents the spatial distribution of LOS parameters and atmospherically corrected TIR imagery during a diurnal cycle. In addition, we compare the results from the spatially distributed atmospheric correction procedure referred to as MLOS (multi line-of-sight) method with a simple approach using non-spatially distributed LOS parameters referred to as SLOS (single line-of-sight) method. Finally, we compare the originally TIR data and the results from the MLOS and SLOS approach with in-situ measurements acquired at one roof in the FOV.

**Atmospheric correction of thermal-infrared imagery**

F. Meier et al.

Title Page

Abstract

Introduction

Conclusions

References

Tables

Figures



Back

Close

Full Screen / Esc

Printer-friendly Version

Interactive Discussion



## 2 Atmospheric effects on oblique TIR imagery in urban areas

This section describes the theoretical background of atmospheric effects on long-wave radiation and demonstrates these atmospheric effects with the help of a fictitious urban setup and radiative transfer simulations using MOD5.

### 2.1 Theoretical background

The radiance  $L_i^{\text{cam}}(\theta_j, z_j)$  recorded in channel  $i$  of a ground-based TIR camera that observes a surface (image pixel  $j$ ) having a certain height a.s.l. ( $z_j^{\text{surf}}$ ) and under view zenith angle ( $\theta_j$ ), is the sum of the surface emission that is attenuated by the atmosphere, the upward radiance emitted by the atmosphere and the radiance from the environment for instance the sky or building walls that is reflected by the ground surface. Under the assumption that the surface is a Lambertian surface, we can write (cf. Sobrino et al., 1991):

$$L_i^{\text{cam}}(\theta_j, z_j^{\text{surf}}) = \int d\lambda f_i(\lambda) \epsilon_\lambda B_\lambda(T) \tau_\lambda(\theta_j, z_j^{\text{surf}}) + \int d\lambda f_i(\lambda) L_\lambda^{\text{atm}}(\theta_j, z_j^{\text{surf}}) + \int d\lambda f_i(\lambda) \frac{1 - \epsilon_\lambda}{\pi} \tau_\lambda(\theta_j, z_j^{\text{surf}}) L_\lambda^{\text{envi}}, \quad (1)$$

where  $f_i(\lambda)$  is the normalized spectral response of the TIR camera in channel  $i$ ,  $\epsilon$  is the surface spectral emissivity,  $B_\lambda$  is the spectral radiance from a blackbody at surface temperature  $T$ , and  $\tau_\lambda$  is the spectral transmission of the atmosphere. The term  $L_\lambda^{\text{atm}}$  in Eq. (1) is the upward atmospheric spectral radiance and is given by:

$$L_\lambda^{\text{atm}}(\theta_j, z_j^{\text{surf}}) = \int_{z_j^{\text{surf}}}^{z_j^{\text{cam}}} dz B_\lambda(T_z) \frac{\delta \tau_\lambda(\theta_j, z_j^{\text{cam}}, z)}{\delta z}, \quad (2)$$

Title Page

Abstract

Introduction

Conclusions

References

Tables

Figures

◀

▶

◀

▶

Back

Close

Full Screen / Esc

Printer-friendly Version

Interactive Discussion





## Atmospheric correction of thermal-infrared imagery

F. Meier et al.

Title Page

Abstract

Introduction

Conclusions

References

Tables

Figures

⏪

⏩

◀

▶

Back

Close

Full Screen / Esc

Printer-friendly Version

Interactive Discussion



the relationship between atmospheric absorption and atmospheric emission. Cold surfaces ( $T_b^{\text{surf}} < T_{\text{air}}$ ) enhance the impact of atmospheric emission, which induced an over-estimation of  $T_b^{\text{surf}}$ . On the other hand, hot surfaces ( $T_b^{\text{surf}} > T_{\text{air}}$ ) enhance the impact of atmospheric absorption, which induces an underestimation of  $T_b^{\text{surf}}$ , here by up to more than 7 K. The expanded range of  $\theta$  for wall B leads to a clear vertical gradient of  $\Delta T_b$  up to 1.2 K ( $T_b^{\text{surf}} = 60^\circ\text{C}$ ). In the case of wall A the vertical gradient of  $\Delta T_b$  is only between 0.1 K ( $20^\circ\text{C}$ ) and 0.5 K ( $60^\circ\text{C}$ ). In the extreme case ( $T_b^{\text{surf}} = 60^\circ\text{C}$ ), the TIR camera records a temperature difference up to 3 K between the bottom of wall A and the top of wall B in spite of equal wall temperature.

The results from this theoretical study emphasise our motivation to develop an atmospheric correction procedure that works on a pixel-by-pixel basis considering the 3-D urban form.

### 3 Materials and method

In the following, we describe the experimental setup, data sets used, the calculation of LOS geometry parameters for every pixel of the TIR image and the atmospheric correction procedure.

#### 3.1 Study site and experimental setup

The study site is located in Berlin (Germany) in the Steglitz-Zehlendorf district ( $52^\circ 27' \text{N}$ ,  $13^\circ 19' \text{E}$ ). City structure is heterogenic and characterized by a five to six-storey block development, two storey residential houses, parks, trees, villas with gardens and one isolated high-rise building (see also Fig. 2a,b). This study is part of a research program called “Energy eXchange and Climates of Urban Structures and Environments (EXCUSE)” that focuses on quantification of energy, momentum and mass exchange processes in the urban boundary layer. In particular, a platform on top of the high-rise building carries a TIR camera system (InfraTec VarioCam head,

7.5–14.0  $\mu\text{m}$ , 320×240 pixels) in order to record the spatial distribution of upward long-wave radiation continuously. For details on technical specifications of the TIR camera system, please see Meier et al. (2010).

During routine operation, the TIR camera records one image per minute. The fixed camera position during this study ensures a valid comparison between the multi-temporal imagery. The experimental setup is supplemented by meteorological measurements on top of the high-rise building (167 m a.s.l.), as well as near-ground instrumentation (66 m a.s.l., see also white circle in Fig. 2) within the FOV of the TIR camera in order to provide humidity and air temperature profile input data for MOD5. Measurement frequency is 5 s for air temperature ( $T_{\text{air}}^{66\text{m}}$ ,  $T_{\text{air}}^{167\text{m}}$ ), relative humidity ( $\text{RH}^{66\text{m}}$ ,  $\text{RH}^{167\text{m}}$ ) devices (Vaisala, HMP45A), which is the right sensor we used to measure air temperature and humidity and downward short-wave radiation ( $\downarrow E_{\text{sw}}^{66\text{m}}$ ,  $\downarrow E_{\text{sw}}^{167\text{m}}$ ) devices (Kipp & Zonen, CM3). Further, we installed one pyrometer measurement device (Heimann, KT15) directly above the roof to obtain in-situ surface brightness temperature ( $T_{\text{b}}^{\text{roof}}$ ) for validation of the atmospheric correction procedure (Fig. 2c, white circle). The pyrometer is located 1 m offset from the roof and observes the roof under the same view zenith angle as the TIR camera.

### 3.2 Pre-processing, radiometric and geometric corrections of TIR imagery

The TIR camera system provides calibration metadata for each recorded image, derived from firmware calibration using laboratory blackbody temperatures. Depending on case temperature, the system generates calibration metadata in a user-defined frequency. The first step of image processing uses these internal calibration parameters for converting measured radiance (digital numbers, DN) into at-sensor brightness temperature  $T_{\text{b}}^{\text{cam}}$  for each pixel. It is possible to convert  $T_{\text{b}}^{\text{cam}}$  into at-sensor radiance  $L_i^{\text{cam}}$  by using the integral of the Planck equation at the sensors wavelengths and weighted by  $f_i(\lambda)$  in order to do further corrections of TIR imagery based on radiance values.

## Atmospheric correction of thermal-infrared imagery

F. Meier et al.

Title Page

Abstract

Introduction

Conclusions

References

Tables

Figures

⏪

⏩

◀

▶

Back

Close

Full Screen / Esc

Printer-friendly Version

Interactive Discussion

### 3.2.1 Vignetting correction

Vignetting refers to the effect of radiance reduction towards the borders of a recorded image relative to its projection centre. The lens itself (aperture effect, pupil aberration) and the parameters of geometric projection of radiance on a non-spherical sensing element (Mitchell, 2010) can cause vignetting. The latter effect is often referred to as the “cosine fourth” law (e.g. Sands, 1973). It refers to the process that on a flat sensing element, uniform radiance is not causing uniform radiance as we move off-axis away from the centre of the image. Those effects are kept to a minimum through optimal design of the lens.

Following the procedure described in Mitchell (2010) we correct empirically for vignetting using a dataset with uniform radiance from a Lambertian source and assuming that the centre of the focal plane array records the correct radiance. We use a dataset with dense fog recorded by the TIR camera system operated at the same location. The dataset was obtained over two minutes on 20 January 2006 from 17:31 to 17:33 Central European Time (CET). Radiance was recorded at 1 Hz and averaged over 120 s to reduce sensor noise. Figure 3a illustrates that  $L_i^{\text{cam}}$  shows a distinct and symmetrical gradient from the centre of the image to the corner. The range  $0.66 \text{ W m}^{-2} \text{ sr}^{-1}$  corresponds to a range in  $T_b^{\text{cam}}$  of approx. 1.5 K. The radiance measured in a rectangular  $6 \times 6$  pixel window in the centre of the image was assumed to be least affected by vignetting and selected as reference radiance  $L_i^{\text{ref}}$ . Figure 3a shows the differences  $\Delta L$  (Eq. 6) for every pixel at row  $x$  and column  $y$ .

$$\Delta L = L_i^{\text{cam}}(x, y) - L_i^{\text{ref}} \quad (6)$$

There is a minor close to linear gradient observed between the top and bottom of the image ( $0.17 \text{ W m}^{-2} \text{ sr}^{-1}$ ) probably due to real atmospheric temperature distribution in the fog. The inclusion of the entire image in the calibration process ensured that this gradient does not affect the calibration. We used a third-order polynomial fit through  $\Delta L$  of all pixels as a function of radial distance (Fig. 3b) in order to correct the radiance

## Atmospheric correction of thermal-infrared imagery

F. Meier et al.

Title Page

Abstract

Introduction

Conclusions

References

Tables

Figures

⏪

⏩

◀

▶

Back

Close

Full Screen / Esc

Printer-friendly Version

Interactive Discussion



for vignetting as a function of radial distance  $\delta$  (in pixels) to the centre pixel:

$$\Delta L = -2.054 \times 10^{-7} \delta^3 + 6.587 \times 10^{-5} \delta^2 - 8.259 \times 10^{-3} \delta + 0.033 \quad (7)$$

The third-order polynomial correction reduces the differences across the image from a root mean square error (RMSE) of  $0.37 \text{ W m}^{-2} \text{ sr}^{-1}$  to  $0.12 \text{ W m}^{-2} \text{ sr}^{-1}$  (unexplained noise). The correction is assumed to be valid for difference radiances measured and has been applied to all imagery prior to geometric and atmospheric correction.

### 3.2.2 Geometric correction

The wide-angle lens that was used produced geometric deformations. These deformations were analysed by measuring a grid of metallic pins in a regular square pattern. We used the positions of the metallic pins to construct a Delaunay triangulation of a planar set of points. Then the geometrical deviations in  $x$ - and  $y$ -direction were interpolated for each image pixel. By using a nearest-neighbour technique, the TIR image pixels can be shifted to their real positions. After correction for lens deformation, the TIR image covers a FOV of  $57.5^\circ$  by  $44.7^\circ$ . Other experiments with TIR cameras using wide-angle lenses (e.g. Lagouarde et al., 2004) also reported such effects.

### 3.3 Spatially distributed line-of-sight (LOS) geometry determination

The determination of spatially distributed LOS geometry parameters is based on digital surface model (DSM) data, photogrammetry and 3-D computer vision techniques. The idea is to link the TIR image pixels to corresponding 3-D coordinates via geometrical transformations used in computer graphics (Foley and van Dam, 1984) based on camera interior and exterior orientation parameters.

At first, we merged the 3-D building vector model, which is available for Berlin in the CityGML format (Kolbe, 2009), and the digital ground model (DGM), which is available in 1 m resolution, into a vector-based DSM. At present, the DSM does not include trees or any other vegetation. Therefore, the atmospheric correction of vegetative TIR pixels

## Atmospheric correction of thermal-infrared imagery

F. Meier et al.

Title Page

Abstract

Introduction

Conclusions

References

Tables

Figures

◀

▶

◀

▶

Back

Close

Full Screen / Esc

Printer-friendly Version

Interactive Discussion



uses LOS parameters representing the nearest underlying ground, wall or roof surface. In order to model the perspective projection of 3-D objects onto the two-dimensional (2-D) TIR image plane, we translate the origin of the DSM coordinate system to the vanishing point of the perspective projection using the following Eq.:

$$\begin{pmatrix} x \\ y \\ z \end{pmatrix} = \begin{pmatrix} X_{\text{DSM}} \\ Y_{\text{DSM}} \\ Z_{\text{DSM}} \end{pmatrix} - \begin{pmatrix} X_{\text{VP}} \\ Y_{\text{VP}} \\ Z_{\text{VP}} \end{pmatrix}, \quad (8)$$

where  $x$ ,  $y$ ,  $z$  are the coordinates in the new camera reference system,  $X_{\text{DSM}}$ ,  $Y_{\text{DSM}}$ ,  $Z_{\text{DSM}}$  are the 3-D coordinates of a point in the originally DSM object space coordinate system and  $X_{\text{VP}}$ ,  $Y_{\text{VP}}$ ,  $Z_{\text{VP}}$  are the 3-D coordinates of vanishing point of the perspective projection, which is the fixed TIR camera position.

The next step defines a view volume in order to realise the interior orientation. In our perspective projection, this is a frustum of a pyramid. Objects that fall within the view volume are projected toward the apex of the pyramid (viewpoint or eye position). Objects that are closer to the viewpoint appear larger because they occupy a proportionally larger amount of the view volume than those that are farther away, in the larger part of the frustum. The bounds of the view volume are described by the FOV parameters of the wide-angle lens of the TIR camera after geometric correction.

The exterior orientation was determined by using the optical centre point ( $P_0$ ) of the TIR image and its coordinates in the camera reference system ( $x_0$ ,  $y_0$ ,  $z_0$ ). Then the view zenith angle ( $\theta_0$ ) between nadir viewing position and  $P_0$  was calculated (Eq. 9) to execute the first rotation of the DSM around the horizontal  $x$ -axis (West–East) of the camera reference system using  $\theta_0$  and 3-D rotation matrix calculation (Foley and van Dam, 1984).

$$\tan(\theta_0) = \frac{\sqrt{x_0^2 + y_0^2}}{|z_0|} \quad (9)$$

**Atmospheric correction of thermal-infrared imagery**

F. Meier et al.

Title Page	
Abstract	Introduction
Conclusions	References
Tables	Figures
⏪	⏩
◀	▶
Back	Close
Full Screen / Esc	
Printer-friendly Version	
Interactive Discussion	



The view azimuth angle ( $\varphi_0$ ) between the horizontal y-axis (North–South) and  $P_0$  was calculated (Eq. 10) to execute the second rotation of the DSM around the vertical z-axis of the camera reference system.

$$\tan(\varphi_0) = \frac{x_0}{y_0} \quad (10)$$

The TIR camera was installed horizontally and allows no tilt around the horizontal y-axis. Hence, a third rotation around this y-axis is not necessary to navigate the DSM into the correct perspective of the TIR camera.

Further, we selected 12 ground control points (GCP) from the DSM data set in order to calculate the RMSE between LOS geometry values derived directly from x, y, z coordinates of GCP and corresponding pixel values of LOS geometry patterns.

### 3.4 Atmospheric correction procedure

The flowchart of the MLOS atmospheric correction procedure is illustrated in Fig. 4. We applied the workflow to 30-min averages of TIR and meteorological data. In order to analyse TST data representing a diurnal cycle, we processed 48 TIR images.

The integrated radiance at the sensor level ( $L_j^{\text{MOD5}}$ ) was simulated for a range of surface brightness temperatures based on air temperature ( $T_b^{\text{MOD5}} \in [T_{\text{air}}^{66\text{m}} - 5\text{K}, T_{\text{air}}^{66\text{m}} + 45\text{K}]$ ) with a 1 K step and a range of LOS parameters with a  $5^\circ$  step for  $\theta$  and a 10 m step for  $z^{\text{surf}}$ , respectively. This set of input parameters provides a reasonable temperature and LOS resolution and takes into account the lower and upper limit of each parameter. The MOD5 atmospheric profile was divided into three levels between  $z^{\text{surf}}$  and  $z^{\text{cam}}$ . Therefore, we used linear interpolated atmospheric profile data  $T_{\text{air}}(z)$  and  $\text{RH}(z)$  derived from the meteorological measurements. Up to now, we only used TIR data from clear-sky days and hence we did not use the cloud options of MOD5.

Overall, 2750 MOD5 runs were used to build-up a LUT for every 30-min interval. Since we know the LOS parameters ( $\theta_j, z_j^{\text{surf}}$ ) for every pixel  $j$ , it is possible to obtain

**Atmospheric correction of thermal-infrared imagery**

F. Meier et al.

Title Page

Abstract

Introduction

Conclusions

References

Tables

Figures

⏪

⏩

◀

▶

Back

Close

Full Screen / Esc

Printer-friendly Version

Interactive Discussion



## Atmospheric correction of thermal-infrared imagery

F. Meier et al.

Title Page

Abstract

Introduction

Conclusions

References

Tables

Figures

⏪

⏩

◀

▶

Back

Close

Full Screen / Esc

Printer-friendly Version

Interactive Discussion



bilinear interpolated LUT values ( $L_j^{\text{bilin}}$ ) on a pixel-by-pixel basis relating the 50 input values of  $T_b^{\text{MOD5}}$  to the simulated at-sensor radiances. Further,  $T_b^{\text{cam}}$  is converted into  $L_j^{\text{cam}}$  by using the integral of the Planck equation at the sensors wavelengths and weighted by  $f_i(\lambda)$  to relate the measured at-sensor brightness temperature to simulated at-sensor radiance. Finally atmospherically corrected surface brightness temperature  $T_b^{\text{surf}}$  is obtained by linear interpolation using  $L_j^{\text{cam}}$  of  $j$ th pixel,  $L_j^{\text{bilin}}$  and  $T_b^{\text{MOD5}}$  (see also Fig. 4).

The SLOS atmospheric correction method is similar to the method described above, but only one LOS parameter pair is used that represents the median of all  $\theta_j$  and the median of all  $z_j^{\text{surf}}$ . Please note, this simple LOS description is already a result of navigating the DSM into the 2-D TIR image projection and cannot be equated with  $\theta_0$  and  $\varphi_0$ . The SLOS method only needs 50 MOD5 runs to do an atmospheric correction of one TIR image.

## 4 Results and discussion

This section presents the spatial distribution of LOS parameters and atmospherically corrected TIR imagery during a diurnal cycle and the 24-hourly average. Further, we show the difference between  $T_b^{\text{cam}}$  and the atmospheric corrections from MLOS ( $T_b^{\text{MLOS}}$ ) and SLOS ( $T_b^{\text{SLOS}}$ ) method and discuss the results from MLOS and SLOS atmospheric correction procedures in relation to in-situ surface brightness temperature ( $T_b^{\text{roof}}$ ) and the magnitude of atmospheric effects in relation to sealed and non-sealed surfaces.

### 4.1 Line-of-sight (LOS) geometry

In the visualizations (Fig. 5), we scaled the values of LOS geometry between 95% percentile (maximum brightness) and 5% percentile (minimum brightness). Furthermore, all grey-scale bars have benchmarks for minimum, median (50%) and maximum value. The same visualisation approach is used for TIR imagery presented in Fig. 6.

## Atmospheric correction of thermal-infrared imagery

F. Meier et al.

Title Page

Abstract

Introduction

Conclusions

References

Tables

Figures

⏪

⏩

◀

▶

Back

Close

Full Screen / Esc

Printer-friendly Version

Interactive Discussion



The perspective projection of the 3-D DSM onto the 2-D image plane is visualized in Fig. 5a. Please note, a wall of the high-rise building carrying the TIR camera is not visible in Fig. 5a, but in the TIR image, we can see this wall in the lower right corner (Fig. 6). This DSM wall polygon object is not visualized, because it is too close to the viewpoint and it lies not fully in the view volume. Thus, the LOS parameters for this wall surface are biased. This surface is excluded from our further analysis. Figure 5b shows the spatial distribution of  $\theta_j$ . The range amounts to  $45.5^\circ$  and is 2.5 times higher than in our fictitious experimental setup (Sect. 2). For the SLOS method, we used the median  $\theta_j$  that amounts to  $60.15^\circ$ . The RMSE between view zenith angles  $\theta_{\text{GCP}}$  derived from 3-D coordinates of the 12 GCP and the corresponding values in the LOS pattern amounts to  $0.8^\circ$ .

Figure 5c shows the spatial distribution of  $z_j^{\text{surf}}$ . The range amounts to 37.1 m, which is approximately 25% of the range in comparison to the fictitious experimental setup. The highest surfaces are the roofs of the five-storey buildings, the church and the roofs in the background located on a small hill. For the SLOS method, we used the median  $z_j^{\text{surf}}$  that amounts to 49.10 m. The RMSE for  $z_j^{\text{surf}}$  is 1.1 m. Overall, the atmospheric path length on the FOV varies between 125.8 m and 773.2 m and the RMSE is 2.9 m (Fig. 5d).

### 4.2 Diurnal cycle of multi line-of-sight (MLOS) atmospherically corrected TIR imagery

We present atmospherically corrected TST data from 8 August 2009 at 06:00 (Fig. 6a), 12:00 (Fig. 6b), 18:00 (Fig. 6c) and 24:00 CET (Fig. 6d). All time specifications refer to CET and the end of the 30-min averaging period. The 24-hourly mean pattern is presented in Fig. 6e and to facilitate interpretability a corresponding photograph of the study site is added (Fig. 6f).

## Atmospheric correction of thermal-infrared imagery

F. Meier et al.

Title Page

Abstract

Introduction

Conclusions

References

Tables

Figures

⏪

⏩

◀

▶

Back

Close

Full Screen / Esc

Printer-friendly Version

Interactive Discussion

During this day, clear sky conditions caused high downward short-wave irradiance with a maximum of  $800 \text{ W m}^{-2}$  around noon. The daily mean  $T_{\text{air}}^{66\text{m}}$  was  $21.2^\circ\text{C}$ , the maximum value reached  $26.1^\circ\text{C}$  at 17:00 and the minimum reached  $16.5^\circ\text{C}$  at 05:00. During daytime, trees and shadowed surfaces have the lowest temperatures. In contrast, roofs, sunlit walls and street surfaces show the highest temperatures, for instance several roofs reaching more than  $50^\circ\text{C}$  at 12:00 (Fig. 6b red coloured surfaces).

During night-time, TIR patterns are dominated by roofs and lawn showing the lowest temperatures and in contrast walls and sealed surfaces have the highest temperatures. The trees are in the medium range showing slightly higher temperatures than roof surfaces. In the 24-hourly mean pattern the order from low to high temperatures is as follows: shadowed lawn, trees, building walls, sealed surfaces and roofs (Fig. 6e).

### 4.3 Multi line-of-sight (MLOS) versus single line-of-sight (SLOS) approach

A visualization approach using fixed colour bars allows interpretation of differences in TIR patterns. Therefore, the values for image scaling (Fig. 7) are derived from all three TIR images showing the difference between  $T_{\text{b}}^{\text{cam}}$  and  $T_{\text{b}}^{\text{MLOS}}$  (left column), the difference between  $T_{\text{b}}^{\text{cam}}$  and  $T_{\text{b}}^{\text{SLOS}}$  (middle column) and the difference between the two atmospheric correction methods ( $T_{\text{b}}^{\text{MLOS}} - T_{\text{b}}^{\text{SLOS}}$ , right column), representing the same 30-min periods as in Fig. 6. The box on the right side of every image plot shows the range of individual image values in order to allow quantitative comparison.

During daytime (Fig. 7b,c) MLOS atmospheric correction reveals that at-sensor values are consistently lower than  $T_{\text{b}}^{\text{MLOS}}$ . There is a clear spatial gradient showing a greater difference for surfaces located further away from the TIR camera. This is particularly notable for very hot surfaces. For instance, underestimation of roof surfaces in the background reaches up to  $7.7 \text{ K}$  at 12:00. The SLOS method also reveals a similar at-sensor underestimation depending on surface temperature (up to  $4.6 \text{ K}$  at 12:00) but a spatial gradient is not visible. The comparison of both atmospheric correction methods (Fig. 7b, right column) shows a clear spatial gradient where the MLOS

values are higher (up to 4.3 K) in the background and lower in the foreground (up to 1.5 K).

During night-time and immediately after sunrise atmospheric effects are much lower than during daytime. The difference between  $T_b^{\text{cam}}$  and the two atmospheric correction methods at 24:00 only varies between  $-0.2$  K (5% percentile) and  $0.4$  K (95% percentile). The TIR camera overestimates cold surfaces ( $T_b^{\text{surf}} < T_{\text{air}}$ ) e.g. for roofs furthest away from sensor and underestimates hot surfaces ( $T_b^{\text{surf}} > T_{\text{air}}$ ) in the case of roads and walls whereas the MLOS pattern (Fig. 7d, left column) reveals the clear dependency on atmospheric path length. This spatial gradient is not visible in the SLOS pattern (Fig. 7d, middle column). However, the differences between MLOS and SLOS are very low (Fig. 7d, right column). The 24-hourly patterns are similar to the daytime patterns but with an overall lower magnitude.

#### 4.4 In-situ data comparison

The comparison between  $T_b^{\text{roof}}$  and the corresponding remote sensing data (roof pixel) shows that the in-situ temperatures are consistently higher than  $T_b^{\text{cam}}$  with the exception of a short period in the morning between 08:30 and 09:30 (Fig. 8). The difference between  $T_b^{\text{roof}}$  and  $T_b^{\text{cam}}$  is clearly reduced due to atmospheric correction, whereas the MLOS method produces a RMSE of 1.69 K and the SLOS method a RSME of 1.84 K (Fig. 9c,d). The deviation of the roof LOS geometry parameters ( $\theta_j = 70.1^\circ$ ,  $z_j^{\text{surf}} = 60.5$  m) from the SLOS input parameters used for MOD5 simulations caused the difference between MLOS and SLOS with a maximum of 0.9 K at 11:00 (Fig. 8b).

In our case, the comparison to in-situ data is critical, because the examined roof is not a strictly homogenous surface. The roof structure produces micro-scale temperature patterns due to tiles self-shadowing and shadow from the measurements installations. This is important for the small FOV ( $9^\circ$ ) of the in-situ KT15 device installed very close (1 m) to the pitched roof resulting in a target area of  $0.03$  m<sup>2</sup>. If we consider the distance of 310 m between roof and TIR camera then the geometric resolution of a roof

### Atmospheric correction of thermal-infrared imagery

F. Meier et al.

Title Page

Abstract

Introduction

Conclusions

References

Tables

Figures

⏪

⏩

◀

▶

Back

Close

Full Screen / Esc

Printer-friendly Version

Interactive Discussion



pixel amounts to 1.1 m. Thus, the FOV of the in-situ measurements covers only 3% of the TIR camera pixel. The values between 08:30 and 09:30 are excluded from the correlation and RMSE analysis (Fig. 9b,c,d).

In April 2010, we moved the TIR camera from the high-rise building and conducted an instrument comparison experiment in the garden of our institute over a 10-day period using a homogenous wood plate as target surface. The data from this experiment reveals that the KT15 device in comparison to the TIR camera produces consistently higher values (Fig. 9a).

#### 4.5 Atmospheric effects regarding sealed and non-sealed surfaces

Now, we use the atmospheric path length as a representative parameter of LOS geometry variability in order to discuss atmospheric effects for different urban surface types. The fictitious experimental setup and results presented in Sect. 4.3 reveal that the atmospheric correction is sensitive to the surface-to-air temperature difference. Hence, we discuss atmospheric effects at 12:00 for two surface types derived from image masks. That are sealed surfaces (roofs, walls and roads) to account for hot surfaces and 108 selected tree crowns, because we expect that tree surface temperature is close to air temperature (Oke, 1987; Leuzinger et al., 2010).

The atmospheric effects ( $T_b^{\text{cam}} - T_b^{\text{MLOS}}$ ) relating to sealed surfaces are shown in Fig. 10a. The atmospheric correction clearly depends on the distance between TIR camera and sealed surface. If we use the SLOS method, this effect produces a strong bias (Fig. 10c). With distance less than 230 m, the atmospheric correction using the SLOS method would produce a warm bias (up to 1.5 K) and from a distance of 230 m to the maximum path length, a cold bias (up to 4.3 K) is expected.

The atmospheric effects relating to tree crowns are shown in Fig. 10b,d. The dependence on path length is present, but  $T_b^{\text{cam}} - T_b^{\text{MLOS}}$  is in the range of 1 K for 95.2% of the tree crown pixels. The slope of a linear regression between atmospheric effect and atmospheric path length (Fig. 10b) is only  $-0.0014 \text{ K m}^{-1}$ . Therefore, the influence of

**Atmospheric correction of thermal-infrared imagery**

F. Meier et al.

Title Page

Abstract

Introduction

Conclusions

References

Tables

Figures



Back

Close

Full Screen / Esc

Printer-friendly Version

Interactive Discussion



incorrect tree LOS geometry parameters due to missing information in the DSM is negligible. The SLOS method produces only a small warm bias up to 0.1 K (5% percentile) and the cold bias is up to 0.4 K (95% percentile) (Fig. 10d). This quantification is based on the 5% and 95% percentile data, because the extreme values are prone to represent non-tree crown pixels due to the porous tree crown or due to falsely classified pixels during the creation of the tree crown mask by visual interpretation of photographs and TIR imagery.

## 5 Conclusions

The study shows that atmospheric correction of ground-based TIR imagery of the 3-D urban environment acquired in oblique viewing geometry has to account for spatial variability of LOS geometry. The combination of 3-D city models, DGM data and 3-D computer vision techniques allow a pixel-by-pixel determination of LOS geometry parameters used for atmospheric correction. In this study the magnitude of atmospheric effects is up to 7.7 K (Fig. 7b, left column) and particularly notable for surfaces showing a strong surface-to-air temperature difference which is typical for urban environments (Voogt and Oke, 2003). The 24-hourly mean pattern shows atmospheric effects up to 2.6 K (Fig. 7e, left column). The applied MLOS atmospheric correction method reveals that the magnitudes of atmospheric effects are biased up to 4.3 K at 12:00 (Fig. 7b, right column) and up to 0.6 K (Fig. 7d, right column) at 24:00, if only the median LOS parameters are used.

An accurate determination of urban surface temperatures via thermal remote sensing is important for sensible heat flux calculations (Voogt and Grimmond, 2000) or the evaluation of surface heat island mitigation measures for instance the conversion of asphalt-covered parking areas to grass-covered ones (Takebayashi and Moriyama, 2009). Atmospheric effects are small for vegetative, shadowed surfaces and trees, but even a 1 K difference can be important for the study of surface temperature variability in relation to tree species or location within the city (Kjelgren and Montague, 1998;

### Atmospheric correction of thermal-infrared imagery

F. Meier et al.

Title Page

Abstract

Introduction

Conclusions

References

Tables

Figures



Back

Close

Full Screen / Esc

Printer-friendly Version

Interactive Discussion







## Atmospheric correction of thermal-infrared imagery

F. Meier et al.

Title Page

Abstract

Introduction

Conclusions

References

Tables

Figures

⏪

⏩

◀

▶

Back

Close

Full Screen / Esc

Printer-friendly Version

Interactive Discussion



- Masson, V., Gomes, L., Pigeon, G., Liousse, C., Pont, V., Lagouarde, J.-P., Voogt, J., Salmond, J., Oke, T., Hidalgo, J., Legain, D., Garrouste, O., Lac, C., Connan, O., Briottet, X., Lachrade, S., and Tulet, P.: The Canopy and Aerosol Particles Interactions in Toulouse Urban Layer (CAPITOU) experiment, *Meteorol. Atmos. Phys.*, 102, 135–157, 2008. 5672
- 5 Meier, F., Scherer, D., and Richters, J.: Determination of persistence effects in spatio-temporal patterns of upward long-wave radiation flux density from an urban courtyard by means of time-sequential thermography, *Remote Sens. Environ.*, 114, 21–34, 2010. 5673, 5679
- Mestayer, P. G., Durand, P., Augustin, P., Bastin, S., Bonnefond, J. M., Benech, B., Campistron, B., Coppalle, A., Delbarre, H., Dousset, B., Drobinski, P., Druilhet, A., Frejafon, E., Grimmond, C. S. B., Groleau, D., Irvine, M., Kergomard, C., Kermadi, S., Lagouarde, J. P., Lemonsu, A., Lohou, F., Long, N., Masson, V., Moppert, C., Noilhan, J., Offerle, B., Oke, T. R., Pigeon, G., Puygrenier, V., Roberts, S., Rosant, J. M., Said, F., Salmond, J., Talbaut, M., and Voogt, J.: The urban boundary-layer field campaign in Marseille (UBL/CLU-ESCOMPTE): set-up and first results, *Bound.-Layer Meteorol.*, 114, 315–365, 2005. 5672
- 10 15 Mitchell, H. B.: *Image Fusion. Theories, Techniques and Applications*, 1st edition, Springer, Berlin, 2010. 5680
- Oke, T. R.: *Boundary Layer Climates*, 2nd edition, Routledge, London, 1987. 5688
- Prata, A. J., Caselles, V., Coll, C., Sobrino, J. A., and Otlé, C.: Thermal remote sensing of land surface temperature from satellites: Current status and future prospects, *Remote Sens. Rev.*, 12, 175–224, 1995. 5673
- 20 Price, J. C.: Land surface temperature measurements from the split window channels of the NOAA-7 advanced very high-resolution radiometer, *J. Geophys. Res.-Atmos.*, 89, 7231–7237, 1984. 5673
- Richter, R. and Schläpfer, D.: Geo-atmospheric processing of airborne imaging spectrometry data, Part 2: atmospheric/topographic correction, *Int. J. Remote Sens.*, 23, 2631–2649, 2002. 5673
- 25 Rotach, M., Vogt, R., Bernhofer, C., Batchvarova, E., Christen, A., Clappier, A., Feddersen, B., Gryning, S.-E., Martucci, G., Mayer, H., Mitev, V., Oke, T., Parlow, E., Richner, H., Roth, M., Roulet, Y.-A., Ruffieux, D., Salmond, J., Schatzmann, M., and Voogt, J.: BUBBLE – an urban boundary layer meteorology project, *Theor. Appl. Climatol.*, 81, 231–261, 2005. 5672
- 30 Sands, P. J.: Prediction of vignetting, *J. Opt. Soc. Am.*, 63, 803–805, 1973. 5680
- Schmugge, T., Hook, S. J., and Coll, C.: Recovering surface temperature and emissivity from thermal infrared multispectral data, *Remote Sens. Environ.*, 65, 121–131, 1998. 5673

## Atmospheric correction of thermal-infrared imagery

F. Meier et al.

Title Page

Abstract

Introduction

Conclusions

References

Tables

Figures

◀

▶

◀

▶

Back

Close

Full Screen / Esc

Printer-friendly Version

Interactive Discussion



Sobrino, J. A., Coll, C., and Caselles, V.: Atmospheric correction for land surface temperature using NOAA-11 AVHRR channel 4 and channel 5, *Remote Sens. Environ.*, 38, 19–34, 1991. 5673, 5675

Sugawara, H., Narita, K., and Mikami, T.: Estimation of effective thermal property parameter on a heterogeneous urban surface, *J. Meteorol. Soc. Jpn.*, 79, 1169–1181, 2001. 5673, 5674

Takebayashi, H. and Moriyama, M.: Study on the urban heat island mitigation effect achieved by converting to grass-covered parking, *Sol. Energy*, 83, 1211–1223, 2009. 5689

Voogt, J. A. and Grimmond, C. S. B.: Modeling surface sensible heat flux using surface radiative temperatures in a simple urban area, *J. Appl. Meteorol.*, 39, 1679–1699, 2000. 5689

Voogt, J. A. and Oke, T. R.: Effects of urban surface geometry on remotely-sensed surface temperature, *Int. J. Remote Sens.*, 19, 895–920, 1998. 5672

Voogt, J. A. and Oke, T. R.: Thermal remote sensing of urban climates, *Remote Sens. Environ.*, 86, 370–384, 2003. 5672, 5673, 5689

Weng, Q. H.: Thermal infrared remote sensing for urban climate and environmental studies: methods, applications, and trends, *ISPRS J. Photogramm.*, 64, 335–344, 2009. 5672

Yang, L. and Li, Y.: City ventilation of Hong Kong at no-wind conditions, *Atmos. Environ.*, 43, 3111–3121, 2009. 5673, 5674

## Atmospheric correction of thermal-infrared imagery

F. Meier et al.

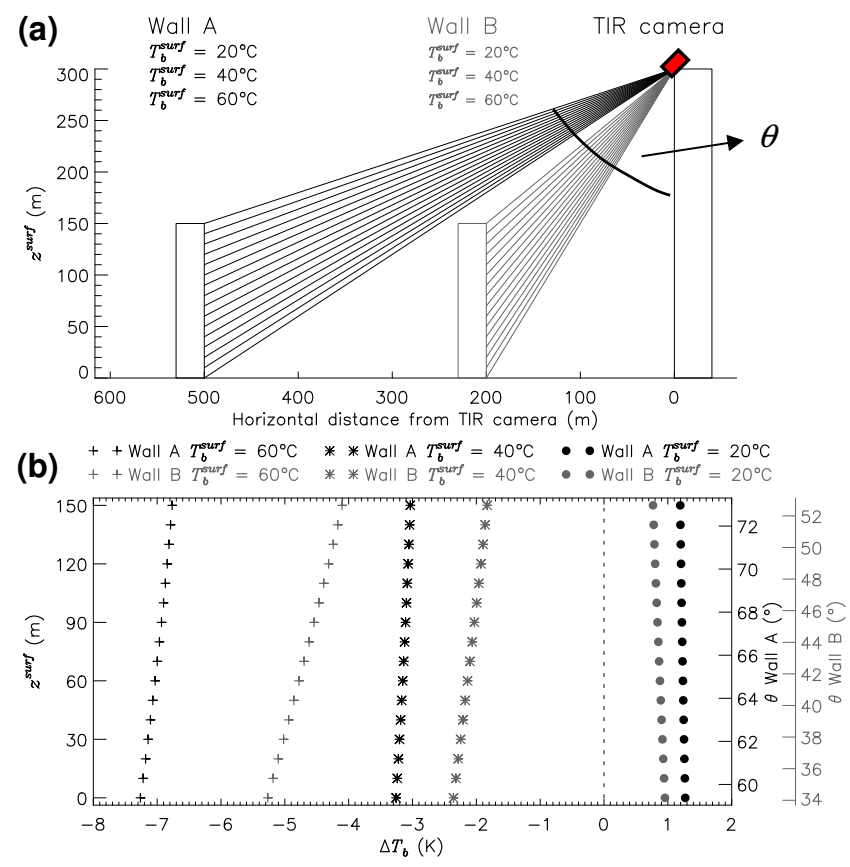


**Fig. 1.** (a) Scheme of the fictitious experimental setup and line-of-sight (LOS) geometry in order to demonstrate atmospheric effects on oblique TIR imagery in urban areas, (b) vertical profiles of  $\Delta T_b$  for wall A (black) and wall B (grey) against wall height ( $z^{surf}$ ) and corresponding view zenith angle ( $\theta$ ) for wall temperatures  $T_b^{surf}$  of  $20^\circ\text{C}$ ,  $40^\circ\text{C}$  and  $60^\circ\text{C}$ , respectively.

Title Page

Abstract Introduction

Conclusions References

Tables Figures

◀ ▶

◀ ▶

Back Close

Full Screen / Esc

Printer-friendly Version

Interactive Discussion



## Atmospheric correction of thermal-infrared imagery

F. Meier et al.

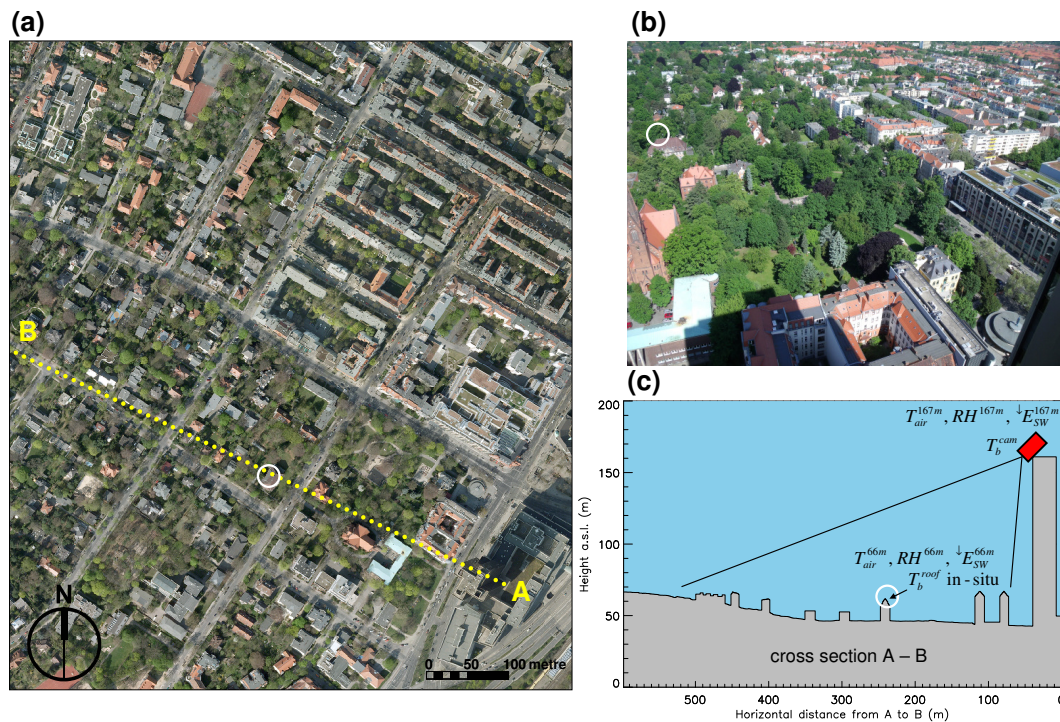


**Fig. 2.** (a) Aerial photo of the study site and ground meteorological measurement site (white circle) (aerial photo with permission of Berlin Department of Urban Development, Urban and Environmental Information System), (b) photograph showing approximately the FOV of TIR camera, (c) cross section A-B illustrates the experimental setup e.g. surface heights, location of TIR camera and in-situ measurements.

Title Page

Abstract

Introduction

Conclusions

References

Tables

Figures

◀

▶

◀

▶

Back

Close

Full Screen / Esc

Printer-friendly Version

Interactive Discussion

## Atmospheric correction of thermal-infrared imagery

F. Meier et al.

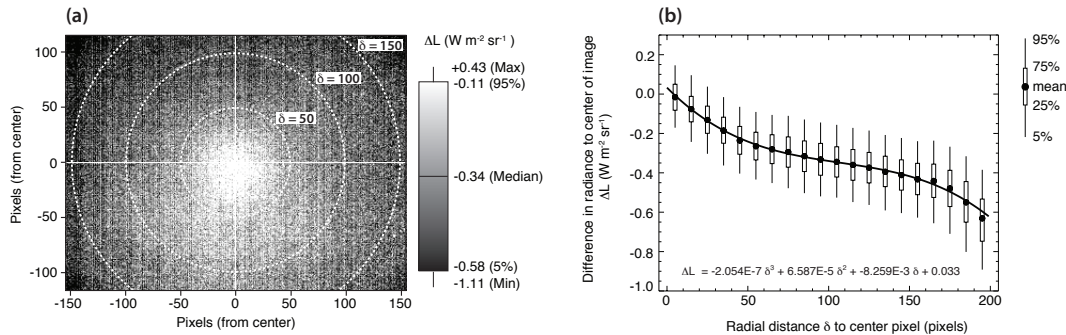


**Fig. 3.** Correction for vignetting: **(a)** Average difference in radiance ( $\Delta L$ ) to the radiance measured in a  $6 \times 6$  pixel window in the centre of the image ( $L_i^{\text{ref}}$ ) during the calibration run in dense fog on 20 January 2006, **(b)** correction derived for vignetting based on all pixels of the image.

Atmospheric correction of thermal-infrared imagery

F. Meier et al.

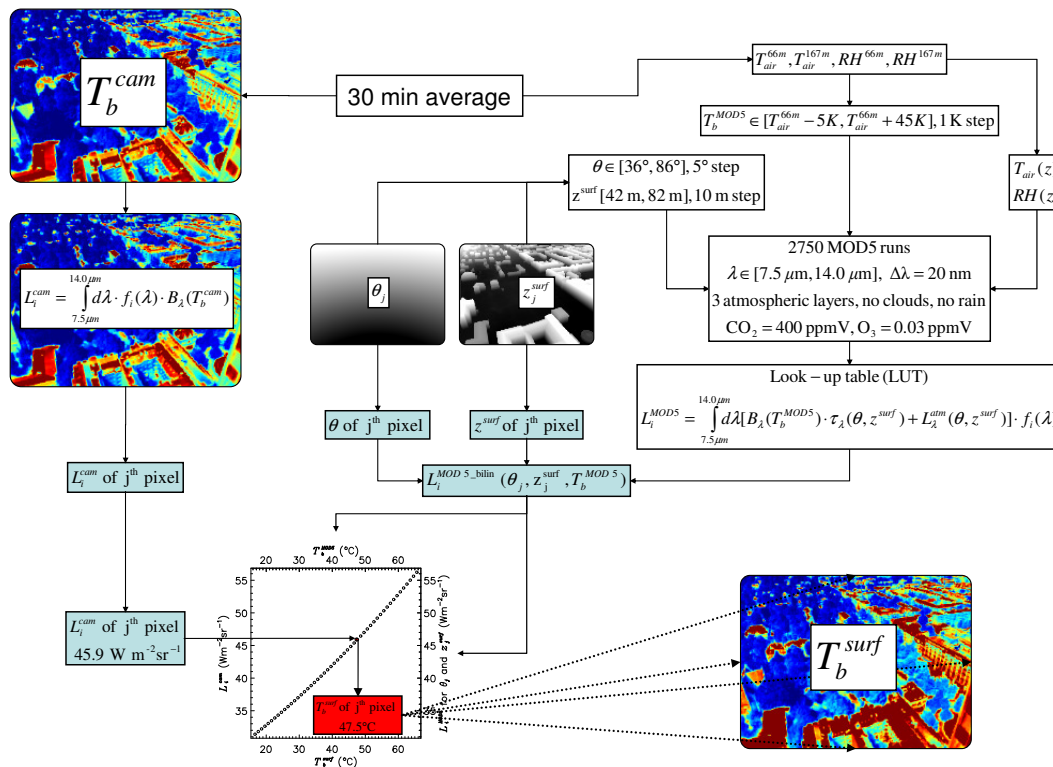


Fig. 4. Flowchart of the multi line-of-sight (MLOS) method on a pixel-by-pixel basis to remove atmospheric effects in off-nadir TIR imagery acquired in an urban environment.

Title Page

Abstract Introduction

Conclusions References

Tables Figures

◀ ▶

◀ ▶

Back Close

Full Screen / Esc

Printer-friendly Version

Interactive Discussion



## Atmospheric correction of thermal-infrared imagery

F. Meier et al.

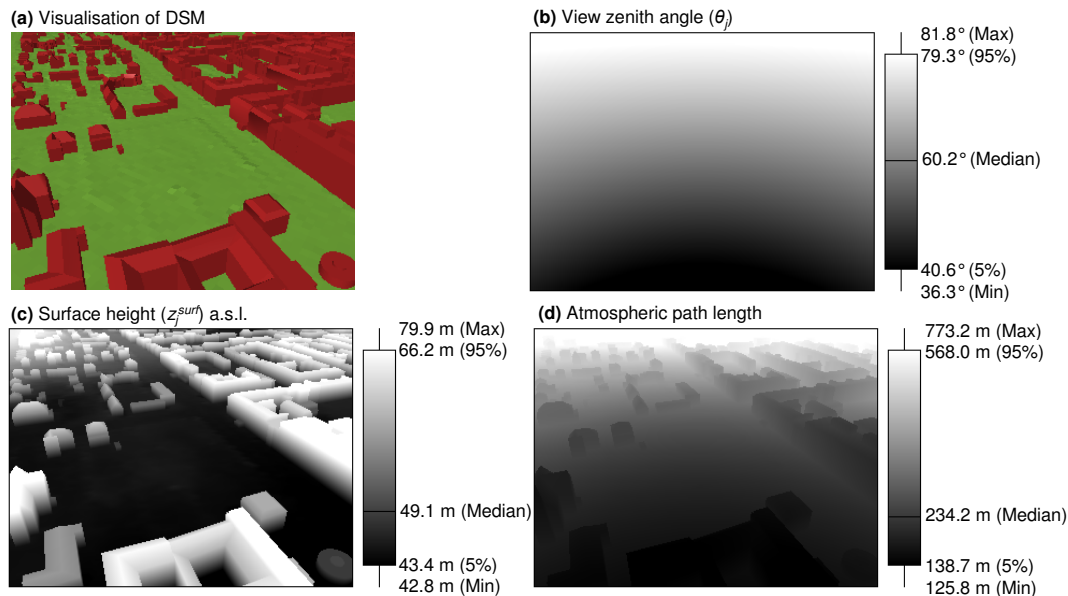


**Fig. 5.** Perspective projection of the DSM, spatial distribution of LOS geometry parameters: **(b)** view zenith angle  $\theta_j$ , **(c)** surface height  $z_j^{\text{surf}}$  and **(d)** atmospheric path length.

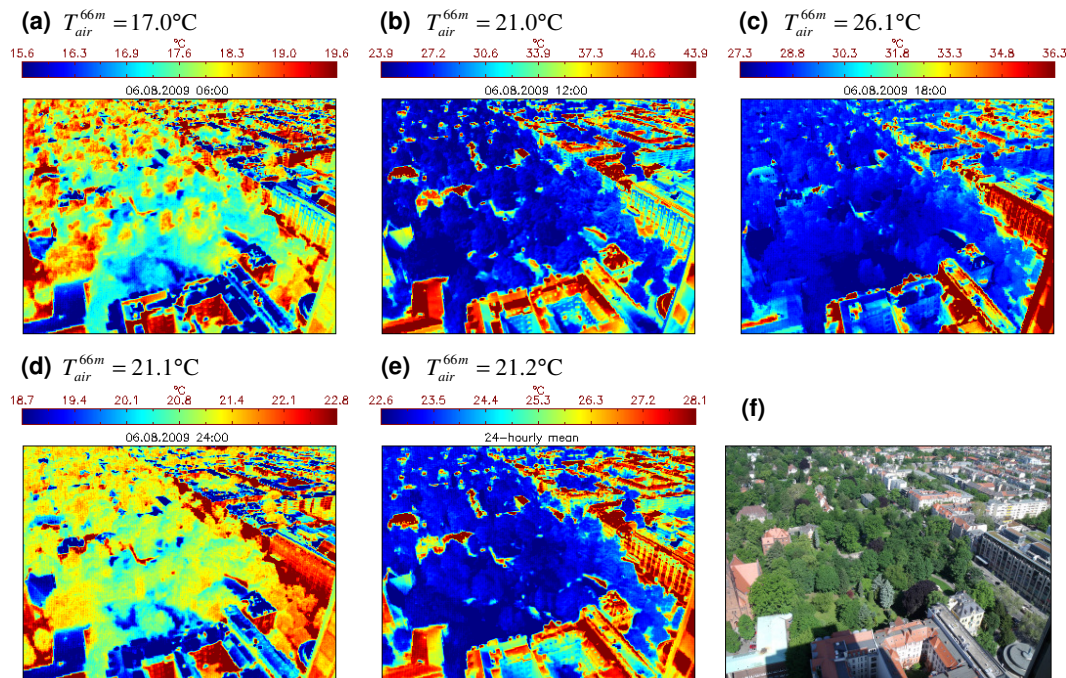


**Fig. 6.** Atmospherically corrected TIR imagery using the MLOS method for selected 30-min periods during 8 August 2009 at 06:00 (a), 12:00 (b), 18:00 (c) and 24:00 (d) CET, the 24-hourly mean pattern (e) and a photograph showing the FOV of TIR camera (f).

## Atmospheric correction of thermal-infrared imagery

F. Meier et al.

Title Page

Abstract

Introduction

Conclusions

References

Tables

Figures

◀

▶

◀

▶

Back

Close

Full Screen / Esc

Printer-friendly Version

Interactive Discussion

## Atmospheric correction of thermal-infrared imagery

F. Meier et al.

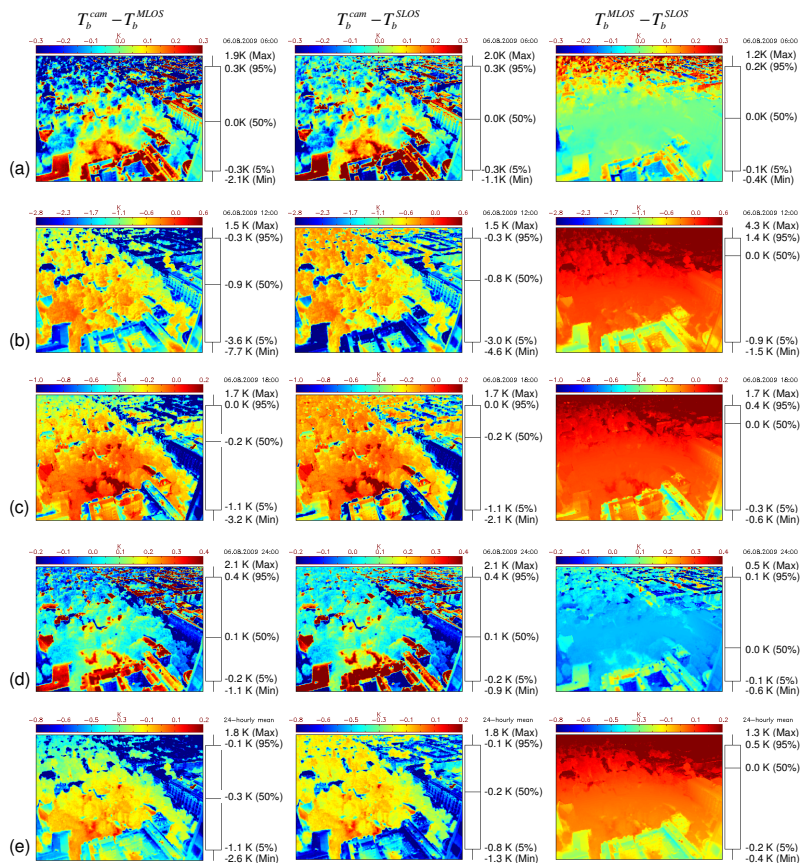


**Fig. 7.** Differences between  $T_b^{\text{cam}}$  and  $T_b^{\text{MLOS}}$  (left column),  $T_b^{\text{cam}}$  and  $T_b^{\text{SLOS}}$  (middle column) and between the two atmospheric correction methods ( $T_b^{\text{MLOS}} - T_b^{\text{SLOS}}$ , right column) for selected 30-min periods during 8 August 2009 at 06:00 (a), 12:00 (b), 18:00 (c) and 24:00 (d) CET and the 24-hourly mean pattern (e).

## Atmospheric correction of thermal-infrared imagery

F. Meier et al.

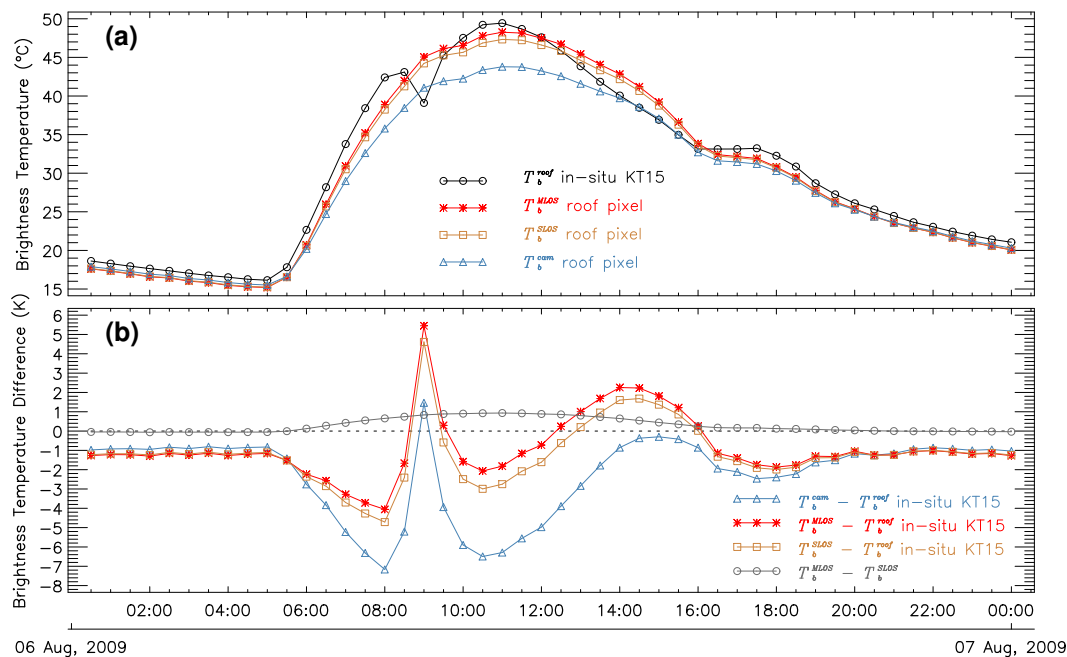


**Fig. 8.** (a) Diurnal variation of  $T_b^{\text{roof}}$  and corresponding TIR remote sensing data (roof pixel) ( $T_b^{\text{cam}}$ ,  $T_b^{\text{MLOS}}$ ,  $T_b^{\text{SLOS}}$ ) during 8 August 2009, (b) temporal variability of difference between  $T_b^{\text{roof}}$  and corresponding TIR remote sensing data and difference between  $T_b^{\text{MLOS}}$  and  $T_b^{\text{SLOS}}$ .

[Title Page](#)
[Abstract](#)
[Introduction](#)
[Conclusions](#)
[References](#)
[Tables](#)
[Figures](#)
[Back](#)
[Close](#)
[Full Screen / Esc](#)
[Printer-friendly Version](#)
[Interactive Discussion](#)

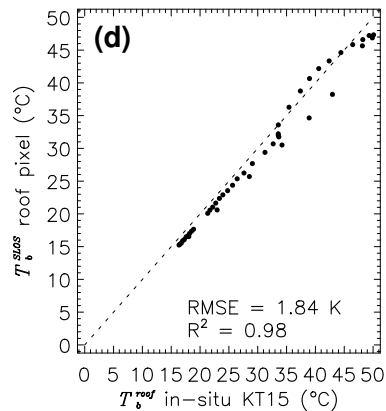
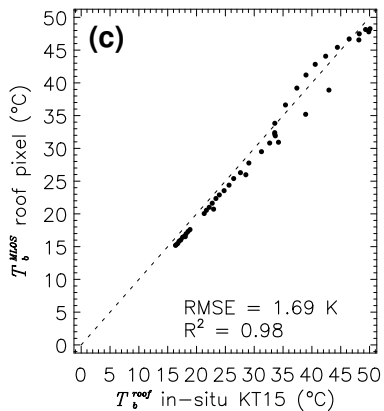
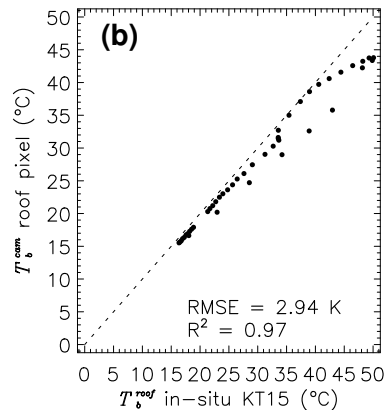
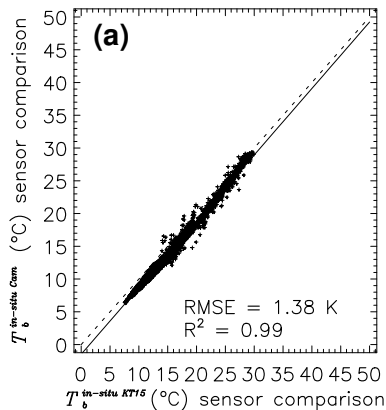


**Fig. 9.** (a) Instrument comparison over 10 days in April 2010 and plots of  $T_b^{\text{roof}}$  in-situ vs. the corresponding remote sensing data (b)  $T_b^{\text{cam}}$ , (c)  $T_b^{\text{MLOS}}$  and (d)  $T_b^{\text{SLOS}}$  during 8 August 2009.

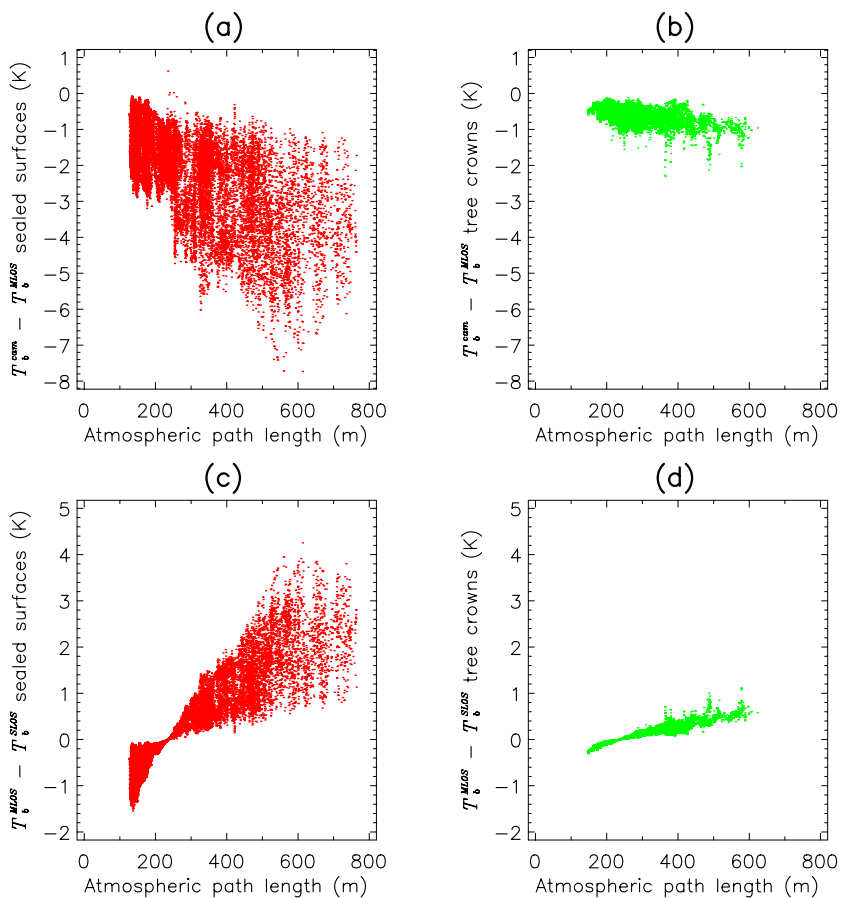


**Fig. 10.** Atmospheric path length vs.  $T_b^{cam} - T_b^{MLOS}$  at 12:00 for **(a)** sealed surfaces and **(b)** tree crowns. Atmospheric path length vs.  $T_b^{MLOS} - T_b^{SLOS}$  at 12:00 for **(c)** sealed surfaces and **(d)** tree crowns.